

Distribution of ~~the~~ Earth's radiation belts protons over the drift frequency of particles

Alexander S. Kovtyukh

Skobeltsyn Institute of Nuclear Physics, Moscow State University, Moscow, 119234, Russia

Correspondence: Alexander S. Kovtyukh (kovtyukhas@mail.ru)

Abstract. ~~On the base of generalized~~ Thanks to the data on the proton fluxes of the Earth's radiation belts (ERB) with energy ranging from ~~$E \sim 0.2$ MeV~~ to 100 MeV at and drift L shells ~~L ranging from ~ 1 to 8,~~ constructed their stationary distributions ~~of the ERB protons~~ over the drift frequency f_d of protons around the Earth are constructed. For this purpose, direct measurements of proton fluxes of the ERB in the period 1961–2017 near the ~~plane of the~~ geomagnetic equator were ~~used~~ employed. The main physical processes in the ERB manifested more clearly in these distributions, and for protons with $f_d > 0.5$ mHz at $L > 3$ their distributions ~~of the ERB protons~~ in the space $\{f_d, L\}$ have a more ~~orderly form~~ regular shape than in the space $\{E, L\}$. It has been found also that the quantity of the ERB protons with $f_d \sim 1$ –10 mHz at $L \sim 2$ does not decrease, as for protons with $E > 10$ –20 MeV (with $f_d > 10$ mHz), but increases with an increase in solar activity. This means that the balance of radial transport and losses of the ERB low-energy protons at $L \sim 2$ is disrupted in advantage of transport: for these protons, the effect of an increase in the radial diffusion rates with increasing ~~in~~ solar activity, overpowers the effect of an increase in the density of the dissipative medium.

Keywords. Magnetospheric physics (energetic particles, trapped). Radiation belts.

24 1 Introduction

25 The Earth's radiation belts (ERB) consist mainly of charged particles with energy from $E \sim 100$
26 keV to several hundreds of megaelectronvolt (MeV). In the field of the geomagnetic trap, each
27 particles of the ERB with energy E and equatorial pitch-angle α_0 (α is the angle between the local
28 vector of the magnetic field and the vector of a particle velocity) makes three periodic movements:
29 Larmor rotation, oscillations along the magnetic field line, and drift around the Earth (Alfvén and
30 Fälthammar, 1963; Northrop, 1963).

31 Three adiabatic invariants (μ , K , Φ) correspond to these periodic motions of trapped particles,
32 as well as three periods of time or three frequencies: a cyclotron frequency f_c , a frequency of
33 particle oscillations along the magnetic field line f_b , and a drift frequency of particles around the
34 Earth f_d . For the near-equatorial ERB protons, ~~these frequencies belong to the following ranges we~~
35 ~~have:~~ $f_c \sim 1\text{--}500$ Hz, $f_b \sim 0.02\text{--}2$ Hz and $f_d \sim 0.1\text{--}20$ mHz. The frequency f_c increases by tens to
36 hundreds of times with the distance of the particle from the plane of the geomagnetic equator (in
37 proportion to the local induction of the magnetic field), and the frequency f_b decreases by almost 2
38 times with increasing ~~the~~ amplitude of particles oscillations.

39 ~~The frequency frequency f_c is different for different L -shells (near the equatorial plane) and as L~~
40 ~~increases it refers to an insignificant number of particles at higher and higher geomagnetic~~
41 ~~latitudes. Each given value of the frequency f_b with increasing L correspond to particles of more~~
42 ~~and more higher energies ($E \propto L^2$) and its value encompass fewer and fewer particles.~~

43 The number of particles with a given frequency f_c decreases rapidly with an increase of L , and
44 refers to higher and higher geomagnetic latitudes. For each given frequency f_b , particles become
45 more and energetic with an increase of L ($E \propto L^2$) and their number becomes smaller.

46 Compared to the frequencies f_c and f_b , the drift frequency f_d ~~of the ERB particles of for~~ one
47 ~~particle~~ species ~~belongs to~~ has a much narrower range of values; ~~the frequency f_d~~ it does not
48 depend on the mass of ~~the~~ particles and it very weakly depends on the amplitude of their
49 oscillations (vary within $\sim 20\%$); ~~in this case, Herein,~~ on each L -shell ~~of the ERB~~ there are a
50 significant number of particles corresponding to a certain value of f_d ~~from a narrow frequency~~
51 ~~range.~~

52 Therefore, it can be expected that the distributions of the ERB particles in the space $\{f_d, L\}$ will
53 have a more ~~orderly regular~~ shape than in the space $\{E, L\}$, and the main physical processes in ~~the~~
54 ~~ERB these belts~~ will manifest themselves more clearly in these distributions. ~~Furthermore,~~ it can
55 also be expected that on these more ordered background ~~will reveal~~ more fine features ~~of the ERB~~
56 ~~can be revealed~~ that ~~do would~~ not appear in the space $\{E, L\}$.

57 ~~Meanwhile, despite~~ Despite the importance of the drift frequency f_d for the mechanisms of the
58 ERB formation, reliable and sufficiently complete distributions of ~~the ERB particles~~ particles in
59 the ERBs (over the frequency f_d) have not been presented ~~and these distributions have not been nor~~
60 analyzed; ~~indeed,~~ this is the first time. ~~This is the first time this is done here.~~

61 ~~For greater reliance, this~~ The analysis presented in this paper is limited ~~here~~ to the protons of
62 the ERB ~~and it is refer to the~~ during magnetically quiet periods of observations, when the ~~proton~~
63 fluxes ~~of the ERB protons~~ and their spatial-energy distributions were stationary. In the following
64 sections, the distributions of the ERB protons over their drift frequency f_d ~~were are~~ constructed ~~by~~
65 ~~the from~~ experimental data (Sect. 2), and ~~these distributions were~~ analyzed (Sect. 3). Finally, the
66 main conclusions of this work are given in Sect. 4.

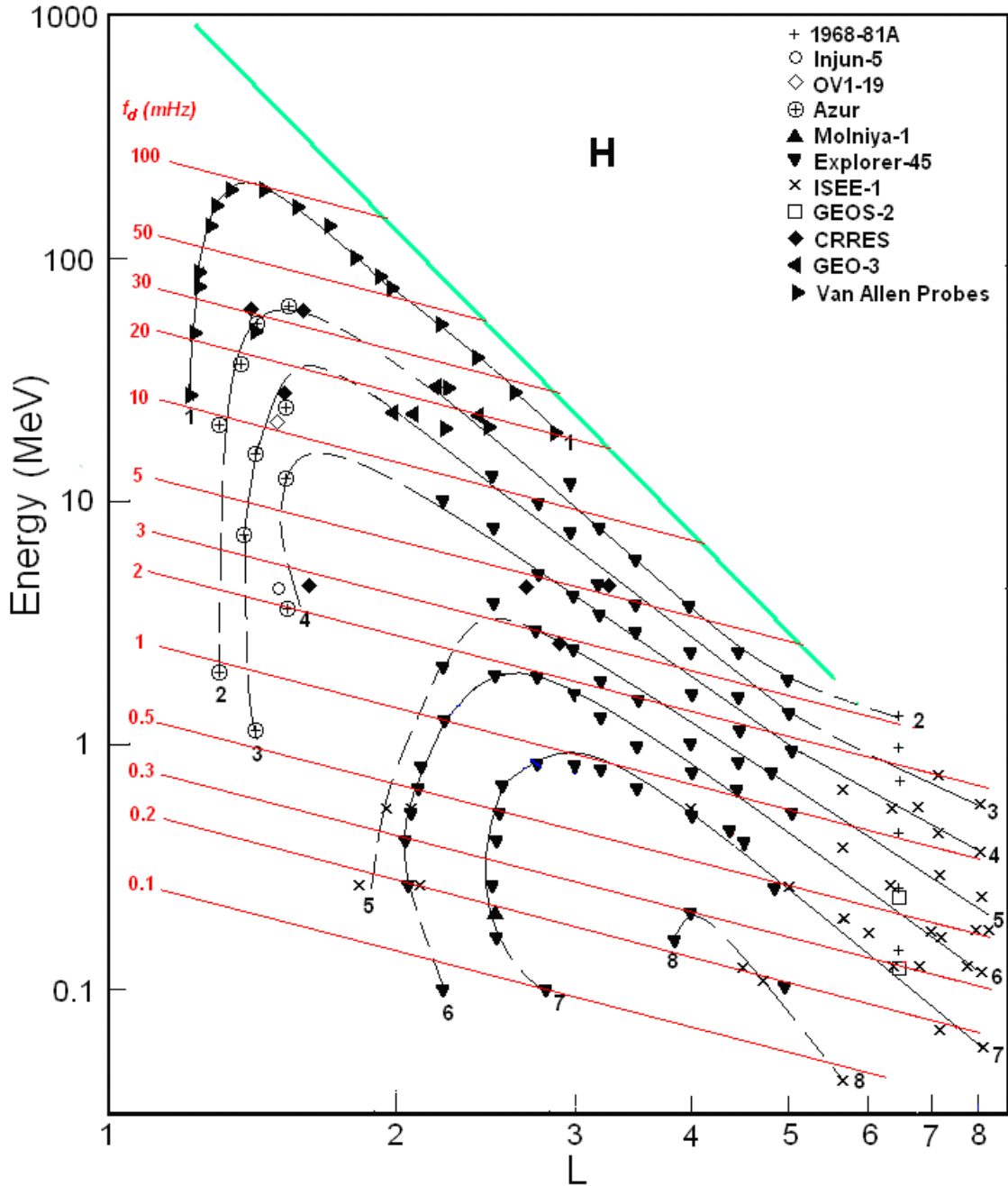
67 2 Constructing the distributions of the ERB protons over their drift frequency

68 2.1 Spatial-energy distributions of the ERB protons near the equatorial plane

69 To construct the distributions of the ERB particles over the drift frequency, it is necessary to have
70 reliable distributions of the differential fluxes of the ERB protons in the space $\{E, L\}$, where E is
71 the kinetic energy of protons and L is the drift shell parameter.

72 ~~According to~~ From the data of ~~generalized and~~ averaged satellite measurements of the
73 differential fluxes of protons with an equatorial pitch-angle $\alpha_0 \approx 90^\circ$, ~~such~~ aforementioned
74 distributions ~~of proton fluxes for quiet conditions is~~ are constructed in (Kovtyukh, 2020) during
75 quiet periods. Such distributions, separately ~~for the~~ between periods near minima and ~~near~~
76 of the 11-year ~~cycles of~~ solar activity cycle, ~~is~~ are constructed from ~~the~~ satellite data also for other
77 ~~main~~ ionic components of the ERB (near the equatorial plane) ~~of the geomagnetic equator~~, but the
78 most reliable and detailed picture was obtained in for ~~a~~ protons (see Kovtyukh, 2020). In Fig. 1 one
79 of these distributions is reproduced; for periods near solar maxima ~~of the solar activity~~ (from 1968
80 to 2017); here, ~~Data~~ data of different satellites are associated ~~in Fig. 1~~ with different symbols.

81 The numbers on the curves (iso-lines) refers to the values of the decimal logarithms of the
82 differential fluxes J ($\text{cm}^2 \text{ s sr MeV}^{-1}$) of protons (with equatorial pitch-angle $\alpha_0 \approx 90^\circ$). The red
83 lines in Fig. 1 corresponds to the dependences $f_d(\text{mHz}) = 0.379 \cdot L \cdot E(\text{MeV})$ for the drift frequency of
84 the near-equatorial protons in the dipole approximation of the geomagnetic field.



85

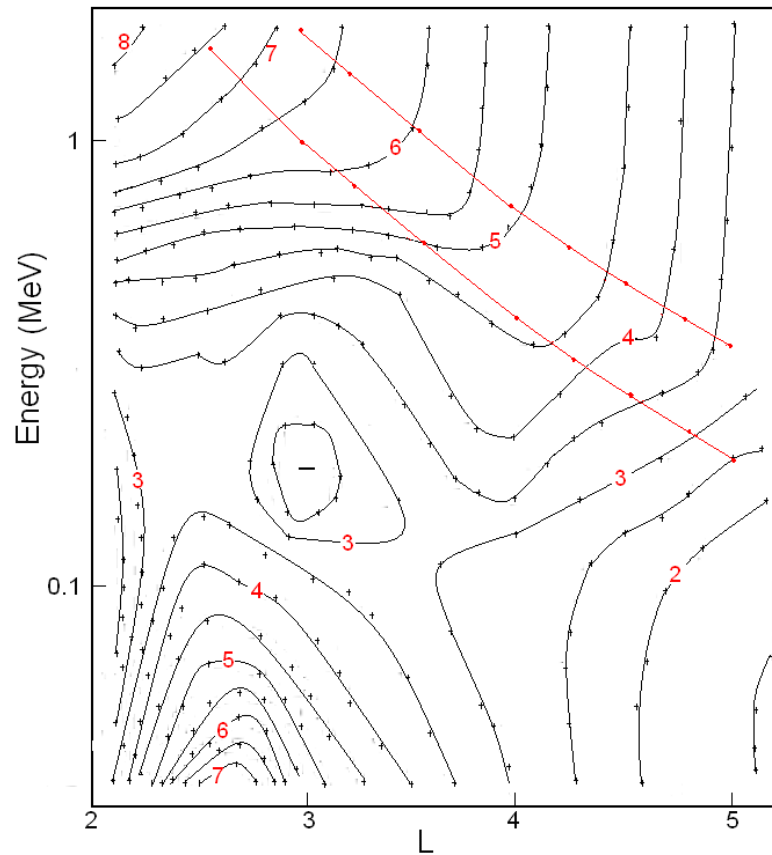
86 **Figure 1.** Distribution of the differential fluxes $J(E, L)$ in the space $\{E, L\}$ for protons with $\alpha_0 \approx 90^\circ$ near maxima of
 87 the solar activity (Kovtyukh, 2020). Data of satellites are associated with different symbols. The numbers on the
 88 curves refers to the values of the decimal logarithms of J . Fluxes is given in units of $(\text{cm}^2 \text{ s sr MeV})^{-1}$. The red lines
 89 correspond to the drift frequency $f_d(\text{mHz})$. The green line corresponds to the maximum energy of the trapped protons.

90 **On the drift shells can be trapped only** Only protons with energies less than some maximum
 91 values, determined by the Alfvén's criterion: $\rho_c(L, E) \ll \rho_B(L)$, where ρ_c is the gyroradius of
 92 protons, and ρ_B is the radius of curvature of the magnetic field (near the equatorial plane) **can be**
 93 **trapped on the drift shells**. According to this criterion and to the theory of stochastic motion of
 94 particles, the geomagnetic trap in the dipolar region can capture and durably hold only protons
 95 with $E (\text{MeV}) < 2000 \cdot L^{-4}$ (Ilyin et al., 1984). The green line in Fig. 1 represents this boundary.

96 The distribution of the ERB proton fluxes shown in Fig. 1, refers to the years of the solar
 97 maximum, but the solar-cyclic variations in the ERB proton fluxes are small and localized at $L <$
 98 2.5 (mainly at $L < 1.4$).

99 **2.2 Spatial-energy distributions of the ERB protons outside the equatorial plane**

100 The stationary fluxes J of the ERB particles with given energy and local pitch-angle α decrease
 101 usually when the point of observation is shifted from the equatorial plane to higher latitudes along
 102 a certain magnetic field line. In the inner regions of the ERB, on $L < 5$, an angular distributions of
 103 protons have usually a maximum at the local pitch-angle $\alpha = 90^\circ$. In wide interval near this
 104 maximum these distributions are well described by the function
 105 $J(\alpha, B/B_0) \propto (B/B_0)^{-A/2} \sin^A \alpha$ (Parker, 1957), where A is the index of an anisotropy of a
 106 fluxes, B is the induction of a magnetic field at the point of measurements of these fluxes and B_0 is
 107 induction of a magnetic field at the equatorial plane on the same magnetic line.



108

109 **Figure 2.** Empirical model of the anisotropy index $A(E, L)$ of the ERB proton fluxes averaged on the data of the
 110 satellites obtained near the plane of the geomagnetic equator. Values of A are given on iso-lines of the anisotropy: $A =$
 111 $1.5-8.5$ with the step $\Delta A = 0.5$.

112 The **generalized** empirical model of an anisotropy $A(E, L)$ for the proton fluxes with $E \sim 0.1-2$
 113 MeV on $L \sim 2-5$ near the equatorial plane for the stationary ERB ($Kp < 2$) is presented in Fig. 2.
 114 The anisotropy index A of ~~the proton~~ these fluxes is shown in Fig. 2, in the space $\{E, L\}$, in the
 115 form of iso-lines with the same values A from 1.5 to 8.0 and with a step $\Delta A = 0.5$. The integer
 116 values of this index are plotted on the corresponding iso-lines ~~in~~ as red numbers.

117 When constructing this model, we consider and analyze the data of the following satellites:
 118 Explorer-12 (Hoffman and Bracken, 1965), Explorer-14 (Davis, 1965), Explorer-26 (Søraas and
 119 Davis, 1968), OV1-14 and OV1-19 (Fennell et al., 1974), Explorer-45 (Williams and Lyons, 1974;
 120 Fritz and Spjeldvik, 1981; Garcia and Spjeldvik, 1985), ISEE-1 (Garcia and Spjeldvik, 1985;
 121 Williams and Frank, 1984), SCATHA (Blake and Fennell, 1981), Van Allen Probes (Shi et al.,
 122 2016), and other satellites. These data were obtained in 1961-2015.

123 **Figure 2** Fig. 2 shows that for rather high energy (> 1 MeV) the anisotropy of a proton fluxes
 124 monotonically increases with decreasing L (from $A \sim 3.5$ to $A \sim 8.0$). For $E > 0.3$ MeV on $L < 3$
 125 anisotropy is monotonically increases with increasing energy, but for $E > 0.5$ MeV on $L > 3$ it is
 126 almost energy-independent **on energy**.

127 Some small irregularities of the iso-lines in Fig. 2 are **connect due** to the fact that experimental
 128 data were used for constructing this figure; these data were obtained in different years, with
 129 different instruments on different orbits of satellites, and during different intensity of the solar
 130 activity. At the same time, Fig. 2 demonstrates the important regularities of the pitch-angle
 131 distributions of the stationary ERB protons.

132 In the region $\{E > 0.5 \text{ MeV}, L > 3\}$ the iso-lines of the anisotropy index are almost parallel to
 133 each other and to the energy **scale axis**. This adiabatic regularity refers **for to** protons belonging to
 134 the power-law tail of their energy spectra, the exponent of which practically does not change when
 135 L changes (at $L > 3$). In Fig. 2, the red lines correspond to the lower boundary of the power-law tail
 136 of the ERB protons energy spectra: $E_b = (36 \pm 11) L^{-3}$ MeV (see Kovtyukh, 2001, 2020).

137 The pattern of $A(E, L)$ in the region on $L > 3$ at $E \sim 0.2\text{--}0.5$ MeV and the local minimum at $L \sim$
 138 3 ($E \sim 0.2$ MeV) are connected with local maximum in the stationary proton energy spectra of the
 139 ERB which corresponds to $E = (17 \pm 3) L^{-3}$ MeV (see Kovtyukh, 2001, 2020).

140 These regularities in the pattern of $A(E, L)$ are explained within the framework of the theory of
 141 radial transport (diffusion) of the ERB protons with conservation of the adiabatic invariants μ and
 142 K of their periodic motions (these **questions issues** were most fully considered in Kovtyukh, 1993).

143 **Local Both the local** maximum at $L \sim 2.5$ ($E < 0.1$ MeV) and the region of low anisotropy at $L \sim$
 144 2 ($E \sim 0.1$ MeV) in Fig. 2, are **connected with related to** the ionization losses of protons.

145 **On the data of the satellites, the pitch-angle distributions of the ERB proton fluxes strongly**
 146 **depend on MLT at $L > 5$: the average index A values on the day side are larger than on the night**
 147 **side, and this dependence becomes more distinct with increasing energy (see, e.g., Shi et al., 2016).**
 148 **These results indicate that drift shells splitting (see Roederer, 1970) play an important role in the**
 149 **formation of these distributions at $L > 5$. In the calculations performed here, it was assumed that**
 150 **near the equatorial plane the pitch-angle distributions of the ERB proton fluxes at $L > 6$, averaged**
 151 **over MLT, at $\alpha_0 \sim 90^\circ$ are nearly isotropic.**

152 High anisotropy for the fluxes of protons at $E = 5\text{--}50$ MeV and a strong dependence $A(L)$ at the
 153 inner boundary of the inner belt ($L = 1.15\text{--}1.40$, $B/B_0 = 1.0\text{--}1.7$) were obtained on the satellite
 154 DIAL (Fischer et al., 1977). According to these data, an anisotropy index increase from $A \sim 12$ at
 155 $L = 1.25$ to $A \sim 60$ at $L = 1.15$, and do not depends on L at $L = 1.25\text{--}1.40$. These results are supported
 156 by the data of the satellite Resurs-01-N4 for the protons with $E = 12\text{--}15$ MeV which **were** obtained
 157 at $h \sim 800$ km (Leonov et al., 2005). They will be taken into account in our calculations.

158 The experimental results on the pitch-angle distributions of the ERB proton fluxes and their
 159 anisotropy indexes were discussed in detail in (Kovtyukh, 2018).

160 2.3 Drift frequency distributions of the ERB protons

161 Based on the results shown in Fig. 1 and 2, one can calculate the distributions of the ERB protons
 162 over the drift frequency f_d . In these calculations, the dipole model of the geomagnetic field was
 163 used, according to which (see, e. g., Roederer, 1970) the point of the magnetic field line at
 164 geomagnetic latitude λ is located from the center of the dipole at a distance

$$165 R(L, \lambda) = R_E L \cos^2 \lambda,$$

166 where R_E is the Earth's radius, and the field induction at a given L changes with changing λ as

167

$$B(L, \lambda) = \frac{\sqrt{4 - 3 \cos^2 \lambda}}{\cos^6 \lambda} B_0(L),$$

168

where $B_0(L) = 0.311 \text{ Gs} \times L^{-3}$.

169

It was also taken into account that the drift frequency f_d of the nonrelativistic particles depends essentially only on their kinetic energy E and on L . This value depends very slightly on the particle pitch-angle: with an increase in the geomagnetic latitude of the mirror point of the particle trajectory from 0 to 10° , it increases by only 1.5%, and in the range from 0 to $20\text{--}30^\circ$ it increases by 5.8–12.5%.

172

The number of protons with energies from E to $E+dE$ per unit volume n is equal to the differential flux of these particles J (falling per unit time per unit area of the detector per unit solid angle), divided by the velocity v of these particles: $n = J/v$. For nonrelativistic protons with mass m , this velocity is $(2E/m)^{1/2}$.

173

174

175

176

Then in the near-equatorial region, between L and $L+dL$ and within geomagnetic latitudes from 0 to $\pm\lambda_0$, the total number of nonrelativistic protons with mirror points within this region and with energy from E to $E+dE$, drifting on a given L with frequency $f_d(L, E)$ around the Earth, is

180

$$\Delta N(L, f_d) = 2 \int_0^{\lambda_0} 2\pi R_E^2 L dL \frac{B_0(L)}{B(L, \lambda)} R_E L \cos \lambda \sqrt{4 - 3 \cos^2 \lambda} d\lambda \times$$

$$4\pi \int_{\alpha_{01}}^{\alpha_{02}} \frac{J(L, E(L, f_d)) dE}{\sqrt{2E(L, f_d)/m}} \sin^A \alpha_0 \cos \alpha_0 d\alpha_0,$$

181

where m is the rest mass of a proton, $J(L, E(L, f_d))$ is the differential fluxes and $E(L, f_d)$ is the protons energy. The first integral takes into account that the magnetic flux in the layer between shells L and

182

183

$L+dL$ is conserved when latitude λ changes, i. e. $2\pi R_E L \cos \lambda R_E dL = 2\pi R_E L \frac{B_0(L)}{B(L, \lambda)} R_E dL$.

184

As result of integrating the last expression over α_0 and replacing $\cos \lambda \equiv t$, we obtain:

185

$$\Delta N(L, f_d) = 4\pi R_E^3 L^2 dL \frac{J(L, E(L, f_d)) dE}{\sqrt{2E(L, f_d)/m}} \times \frac{4\pi}{A+1} \times$$

$$\int_{\cos \lambda_0}^1 t^7 \left[\left(\frac{t^6}{\sqrt{4 - 3t^2}} \right)^{\frac{A+1}{2}} - (0.565)^{A+1} \right] dt$$

186

When integrating over equatorial pitch-angles α_0 , Liouville's theorem and the conservation of the first adiabatic invariant (μ) are taken into account: $\sin^2 \alpha_{01} = B_0(L)/B(L, \lambda_0)$ and $\sin^2 \alpha_{02} = B_0(L)/B(L, \lambda)$, where $B(L, 0) = B_0(L)$.

187

188

189

With an increase λ from 0 to $\lambda_0 = 30^\circ$, the value of the function $\sqrt{4 - 3t^2}$ increases from 1 to 1.32, i.e. deviates from the average value (1.16) by only 16%. Most part of the ERB protons are concentrated at these latitudes. Therefore, when calculating the last integral, we will assume that

190

191

192

$\sqrt{4 - 3t^2} \approx 1.16$.

193

Then you can get the following expression:

194

$$\Delta N(L, f_d) = k \frac{J(L, E(L, f_d))}{\sqrt{E(L, f_d)}} F(A) L^2 dL dE,$$

195 where

196

197

$$F(A) = \frac{1}{A+1} \left[\frac{(1.16)^{-(A+1)/2}}{3A+11} \left(1 - 0.21 \cdot 0.65^A \right) - 0.085 (0.565)^{A+1} \right]$$

198 and

199

$$k = (4\pi)^2 R_E^3 \sqrt{m/2} = 2.945 \cdot 10^{19} \text{ cm}^2 \text{ s sr MeV}^{1/2}.$$

200

When calculating the values of ΔN , we will take that $dL/L = dE/E = 0.1$. Finally, for the indicated ERB region near the equatorial plane, we obtain:

201

202

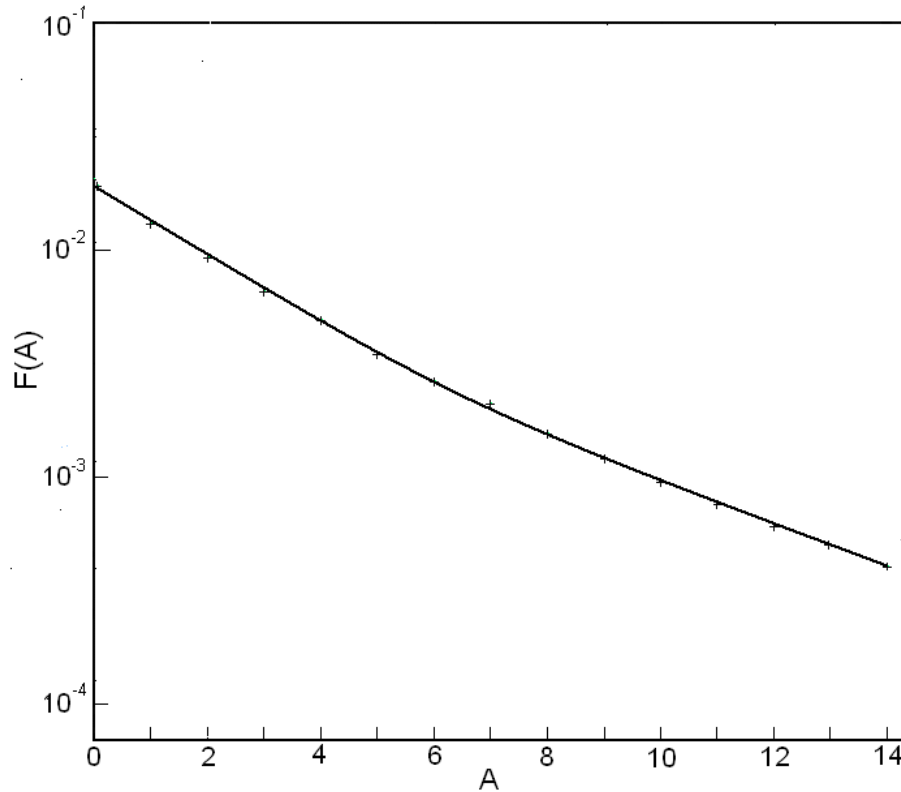
$$\Delta N(L, f_d) = 2.945 \cdot 10^{17} J(L, E(L, f_d)) \sqrt{E(L, f_d)} F(A) L^3, \quad (1)$$

203

where J , the differential fluxes of protons with equatorially pitch-angle $\alpha_0 \approx 90^\circ$, is given in units of $(\text{cm}^2 \text{ s sr MeV})^{-1}$, and the energy of protons E is given in MeV. The dependence $F(A)$ is shown in Fig. 3.

204

205



206

207

Figure 3. Dependence of the factor $F(A)$ in formula (1) on the anisotropy index A of the proton fluxes.

208

209

For protons of the ERB, the radial profiles $\Delta N(L, f_d)$ for $f_d = 0.2, 0.3, 0.5, 1, 2, 3, 5, 10, 20$, and 30 mHz, calculated by using the formula (1) together with using Figs. 1–3 are shown in Fig. 4, and the frequency spectra $\Delta N(f_d, L)$ at $L = 2, 2.5, 3, 4, 5$, and 6 are shown in Fig. 5. Near each curve in Fig. 4, the corresponding value of f_d (mHz) is indicated, and each spectrum in Fig. 5 have the corresponding L value (these values are highlighted in red). For clarity, in Figs. 4 and 5, thin curves alternate with thick curves and in Fig. 5 spectra at $L = 2$ and 2.5 are highlighted in red.

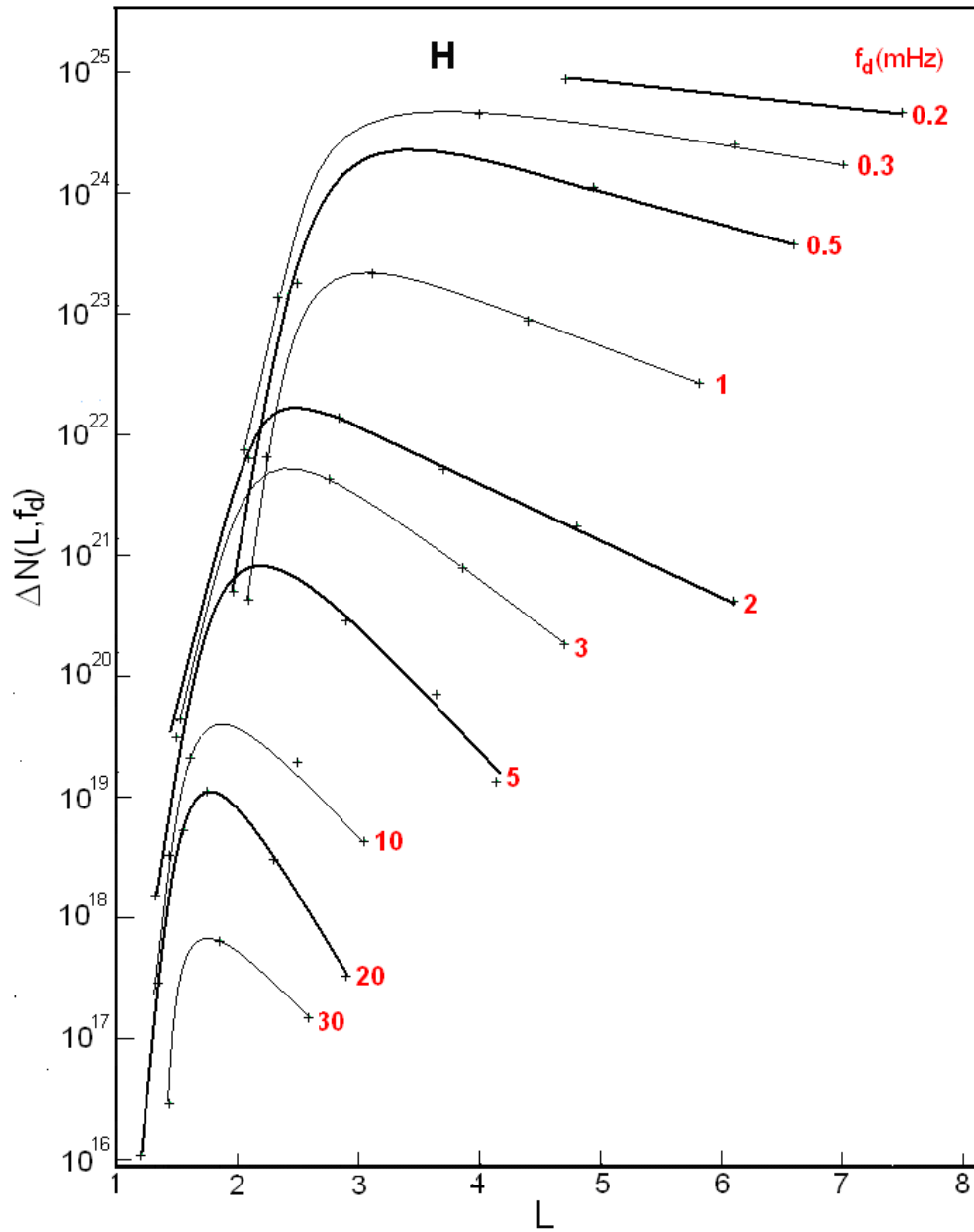
210

211

212

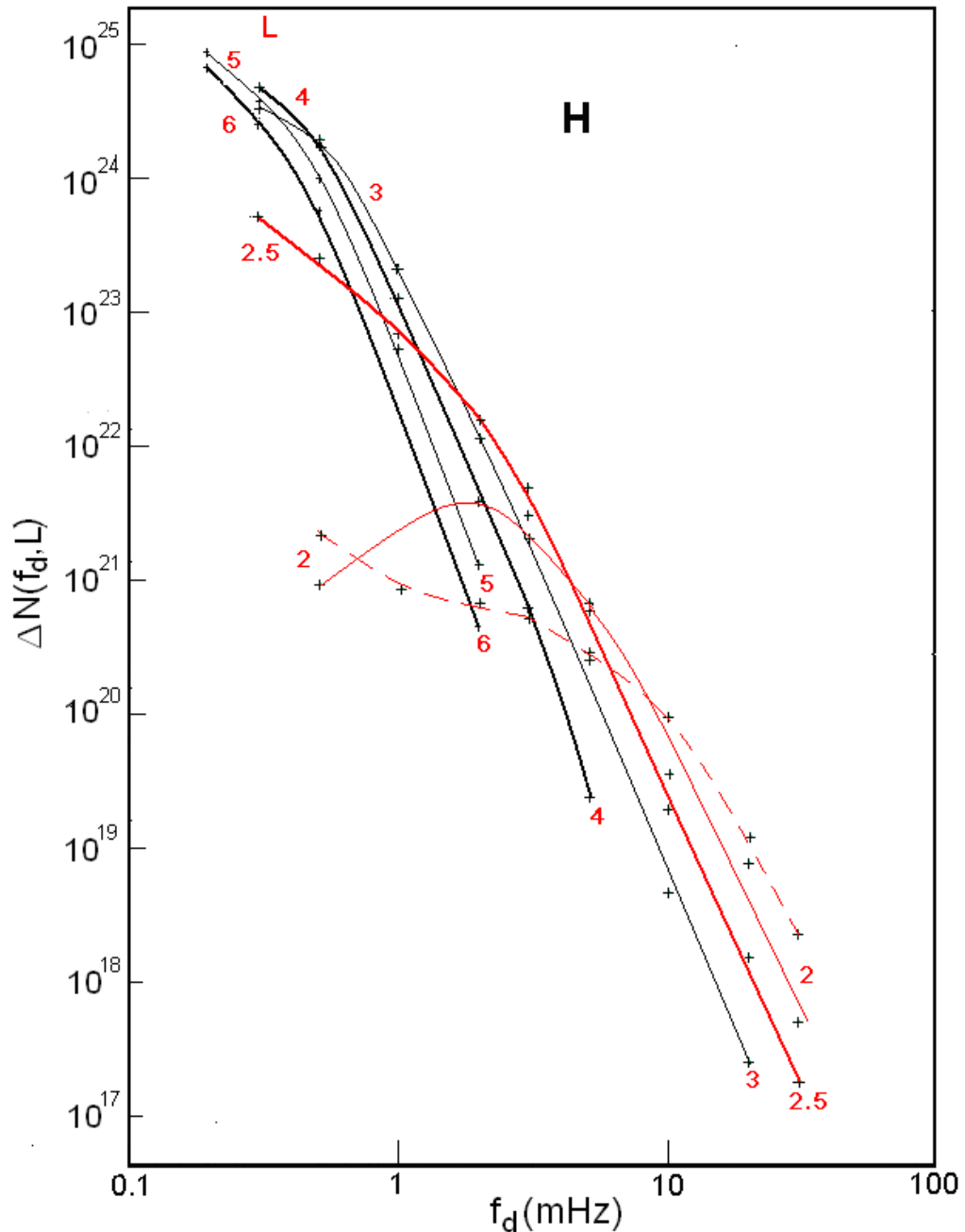
213

214



215

216 **Figure 4.** Radial profiles $\Delta N(L, f_d)$ for protons of the ERB with drift frequencies $f_d = 0.2, 0.3, 0.5, 1, 2, 3, 5, 10, 20$ and
 217 30 mHz, plotted for periods of **maximum** solar activity **maxima**. The f_d values corresponding to each curve are
 218 highlighted in red. For clarity, thin curves are interspersed with thick curves.



219
220
221
222
223
224

Figure 5. Frequency spectra $\Delta N(f_d, L)$ for protons of the ERB at $L = 2, 2.5, 3, 4, 5$ and 6 , plotted for periods of maximum solar activity maxima. The values L corresponding to each spectrum and spectra at $L = 2$ and 2.5 are highlighted in red. The red dotted line shows the spectrum $\Delta N(f_d, L)$ of the ERB protons at $L = 2$, constructed from data for during minimum periods of solar activity minima (see Kovtyukh, 2020). For clarity, thin curves are interspersed with thick curves.

225
226
227

The errors of these calculations consist mainly of the errors of the averaged experimental data shown in Figs. 1 and 2 (these errors are most significant at $L < 2$), and because of the deviations of the geomagnetic field from the dipole model at $L > 5$.

228
229
230
231
232

As λ_0 decreases, the errors in our calculations will decrease. These errors can be reduced also by using numerical computer calculations. However, it should be taken into account that the fluxes of the ERB protons, as well as the energy spectra and pitch-angle distributions of these fluxes, may experience changes that exceed the errors of our calculations even in very quiet periods of observations.

233 3 Discussion

234 In agreement with the results of experimental and theoretical studies, at $L > 2.5$, the main
235 mechanism for the formation of the ERB ~~for~~ protons is the radial diffusion of particles from the
236 outer boundary of the geomagnetic trap to the Earth under conservation the adiabatic invariants μ
237 and K (see, e.g., Lejosne and Kollmann, 2020; Kovtyukh, 2016b, 2018).

238 **Figures** Figs. 1 and 2 presented here make it possible to determine in which regions of the space
239 $\{E, L\}$ near the equatorial plane the ionization losses of ions during their radial diffusion can be
240 neglected and where this cannot.

241 The iso-lines of ~~the~~ proton fluxes in Fig. 1 at sufficiently large E and L go up with decreasing L ,
242 in the direction of increasing energy, in strict agreement with the adiabatic laws of radial transport
243 of particles. At lower L these iso-lines ~~reject deflect to the low energies~~ **do change the direction of**
244 **their course**, under the influence of ionization losses, which increase rapidly with decreasing L (see
245 in Kovtyukh, 2020 for details).

246 At sufficiently large values of E and L , iso-lines of the anisotropy index in Fig. 2 pass
247 practically parallel to each other and parallel to the energy axis, in agreement with the laws of
248 adiabatic transport of particles with power-law energy spectra (see Kovtyukh, 1993). At lower E
249 and L , a more complex picture is formed under the influence of ionization losses (for more details
250 see in Kovtyukh, 2001, 2018).

251 With decreasing L , the radial diffusion ~~are~~ **is** decreased very rapidly, and the belt of protons
252 with $E > 10\text{--}20$ MeV on $L < 2$ is generated mainly as result of decay a neutrons of albedo which
253 are knocked from the atmospheric atoms nuclei by the Galactic Cosmic Rays (GCR) protons. This
254 mechanism (CRAND) is simulated in many contemporary studies based on the experimental data
255 (see, e. g., Selesnick et al., 2007, 2013, 2014, 2018).

256 The mechanisms of formation of the ERB under the action of radial diffusion and CRAND are
257 manifested and clearly differ both in the radial profiles $\Delta N(L, f_d)$ and in the frequency spectra
258 $\Delta N(f_d, L)$ of protons.

259 Let us consider the manifestations of these mechanisms in Fig. 4 and 5 and related effects.

260 In contrast to the radial profiles of fluxes $J(L, E)$, the radial profiles $\Delta N(L, f_d)$ for protons with f_d
261 > 10 mHz (see Fig. 4) have much less ~~steeper of the~~ outer edges and their steepness decreases with
262 decreasing frequency f_d . This effect is connected mainly with an increase in the volume of
263 magnetic tubes (factor L^3 in formula (1) from Section 2.3) and with a decrease in the anisotropy
264 index of proton fluxes with increasing L .

265 At the same time, in comparison with the radial profiles $J(L, E)$, the radial profiles $\Delta N(L, f_d)$
266 have more steeper inner edges. This effect is **mainly** connected ~~mainly with~~ to the large anisotropy
267 of proton fluxes in the corresponding region of space $\{E, L\}$ and with the rapid growth of the
268 anisotropy index with decreasing L in this region. It is especially expressed in the radial profiles
269 $\Delta N(L, f_d)$ at $f_d \sim 0.3\text{--}1$ mHz (see Fig. 4); this is due to the fact that in the corresponding region of
270 space $\{E, L\}$ the anisotropy index of proton fluxes strongly depends on E and L (see Fig. 2).

271 Radial profiles $\Delta N(L, f_d)$ at $f_d > 10$ mHz are formed by the mechanism CRAND. They have a
272 maximum at $L \sim 1.5\text{--}2.0$, and the steepness of their inner and outer edges does not differ as much
273 as for lower frequencies f_d (see Fig. 4). When constructing these profiles, it was taken into account
274 that at $E = 5\text{--}50$ MeV an anisotropy index A of proton fluxes do not depend on L at $L = 1.25\text{--}1.40$:
275 $A = 12 \pm 2$ (Fischer et al., 1977; Leonov et al., 2005).

276 The shape of the spectra $\Delta N(f_d, L)$ at $L > 3$ is determined, first of all, by the shape of the energy
277 spectra of proton fluxes $J(E, L)$ at the outer boundary of the geomagnetic trap. Gradually, as the
278 particles diffuse to the Earth, their energy spectra are transformed under the action of betatron
279 acceleration and ionization losses of particles.

280 In contrast to the energy spectra of proton fluxes $J(E, L)$, distributions $\Delta N(f_d, L)$ of the ERB
 281 protons over their drift frequency f_d (Fig. 5) differ much less from each other at $L > 3$. Such
 282 convergence of the spectra $\Delta N(f_d, L)$ is driven by increase in the volume of magnetic tubes and a
 283 decrease in the anisotropy index of the ERB proton fluxes with increasing L . ~~Figure 5 testify for~~
 284 ~~else~~ Fig. 5 demonstrates the closeness to the adiabatic transformations of the spectra $\Delta N(f_d, L)$
 285 when L changes at $L > 3$.

286 The energy spectra of near-equatorial proton fluxes $J(E, L)$ with $E > 10 \cdot L^{-3}$ MeV at $L > 3$ in
 287 quiet periods have a local maximum at $E = (17 \pm 3) \cdot L^{-3}$ MeV and a power-law tail ($J \propto E^{-\gamma}$, where γ
 288 $= 4.25 \pm 0.75$) at $E > (36 \pm 11) \cdot L^{-3}$ (Kovtyukh, 2001, 2018, 2020).

289 The frequency spectra of the ERB protons at $L > 3$ weakly depend on L and over the considered
 290 range Δf_d have a close to power-law shape with an exponent $\gamma = 4.71 \pm 0.43$ (at $f_d > f_d^*$, where f_d^*
 291 ~ 0.5 mHz at $L \sim 3-6$, ~ 2 mHz at $L = 2.5$ and ~ 5 mHz at $L = 2$). Note that the spread of the
 292 parameter γ for the frequency spectra of protons is almost 2 times less than for their energy spectra.
 293 These spectra become more rigid (flattened) at $f_d < f_d^*$.

294 Thus, the average exponents of the power-law tail of the energy and frequency spectra of
 295 protons differ by $\Delta\gamma = 0.46$, and there is no local maximum in the frequency spectra at $f_d > 2$ mHz
 296 at $L > 2.5$. The main role in such differences in the shape of the energy and frequency spectra of
 297 protons was played by the factor $F(A)$ in formula (1), in which the anisotropy index A is a function
 298 of E and L (see Figs. 2 and 3). Note that in the region $\{E > 0.5 \text{ MeV}, L > 3\}$ the anisotropy index
 299 A , as well as the protons energy, is transformed according to adiabatic laws when L changes (see
 300 Fig. 2 and comments to it).

301 These results confirm our hypothesis about the ordering of the distributions of protons over
 302 their drift frequency f_d in the outer regions of the ERB, at $L > 3$, where most of the ERB protons
 303 are located and where the radial diffusion of protons overpowers their ionization losses.

304 At all L , the frequency spectra $\Delta N(f_d, L)$ become more flat at small f_d and E under influence
 305 ionization losses. However, in the range of high f_d (from 3–5 mHz to 30 mHz), for protons with
 306 high energies and low ionization losses, the protons frequency spectra ~~save~~ have a power-law tail
 307 even at $L = 2$ (see Fig. 5).

308 For protons with $f_d < 0.5$ mHz, which correspond to the ERB protons of the lowest energies,
 309 ionization losses lead to the same consequences at higher L -shells: the radial profiles $\Delta N(L, f_d)$
 310 approach each other, and the spectra $\Delta N(f_d, L)$ flatten out (see Figs. 4 and 5).

311 In the region of the steep inner edge of the radial distributions $\Delta N(L, f_d)$, spectra $\Delta N(f_d, L)$ of the
 312 ERB protons ~~gradually, with decreasing L~~ , become ~~gradually~~ increasingly rigid ~~with decreasing L~~ ,
 313 and rapidly diverge from each other (see Fig. 4 and 5). In the range of small f_d at $L < 2.5$, the
 314 connection between these distributions and the shape of the boundary energy spectra of protons is
 315 gradually lost.

316 These results indicate a violation of the order in the distributions of protons under the influence
 317 of ionization losses.

318 In Fig. 5, the dotted line also shows the spectrum $\Delta N(f_d, L)$ of the ERB protons at $L = 2$,
 319 constructed from experimental data for periods of low solar activity (see Fig. 1 in Kovtyukh,
 320 2020). ~~Figure~~ Fig. 5 show that at $L = 2$ for $f_d > 10$ mHz there were more protons at the minimum of
 321 solar activity, and for $f_d \sim 1-10$ mHz there were more protons at the maximum of solar activity.

322 The effect of a decrease in the $\Delta N(f_d, L)$ values for protons with $f_d > 10$ mHz at $L < 2$ with an
 323 increase in solar activity is mainly connected with a decrease in the fluxes of protons with $E > 10-$
 324 20 MeV here. This effect is well known. It is described by the CRAND mechanism (see, e.g.,
 325 Selesnick et al., 2007) and was considered in detail in (Kovtyukh, 2020). With an increase in solar

326 activity, the densities of atmospheric atoms and ionospheric plasma on small L -shells significantly
327 increase, which leads to an increase in ionization losses of the ERB protons, but the power of their
328 main source (CRAND) practically does not change. As a result, the equilibrium fluxes and $\Delta N(f_d,$
329 $L)$ for protons with $f_d > 10$ mHz are established at lower levels.

330 However, the effect of an increase in $\Delta N(f_d, L)$ for $f_d \sim 1$ – 10 mHz at low L with increasing solar
331 activity, corresponding to the protons of lower energies, was discovered here for the first time.

332 With decreasing E (and f_d) of protons their ionization losses increase, and if the fluxes of
333 low-energy protons in the inner belt were also formed by the CRAND mechanism, one would have
334 observed even stronger increase of their fluxes with decreasing solar activity, than for
335 protons with $E > 10$ – 20 MeV ($f_d > 10$ mHz). But for protons with $f_d \sim 1$ – 10 mHz, we see in Fig. 5
336 reverse the opposite effect in the spectra $\Delta N(f_d, L)$ at $L = 2$, which is not described by the CRAND
337 mechanism.

338 On the other hand, it was proved that stationary fluxes of protons with $E < 15$ MeV at $L \sim 2$ are
339 formed mainly by the mechanism of protons radial diffusion from the external region of the ERB
340 (Selesnick et al., 2007, 2013, 2014, 2018). These fluxes and $\Delta N(f_d, L)$ values for $f_d \sim 1$ – 10 mHz at
341 $L = 2$ are formed as a result of a balance of competing processes radial diffusion of protons and
342 their ionization losses.

343 The rates of transport of the ERB protons to the Earth (radial diffusion) rapidly increase with
344 decreasing particles energy (see Kovtyukh, 1916b). In addition, with an increase in solar activity,
345 the average level of geomagnetic fluctuations in the ERB increases. Under the influence of these
346 factors, one can expect a significant increase in the intensity of radial diffusion of the low-energy
347 protons at low L with an increase in solar activity. As a result, the effect of increasing in the
348 density of a dissipative medium with an increase in solar activity is overpowered by a more
349 significant effect of increasing in the rates of radial diffusion of protons.

350 According to a numerous experimental data, during magnetic storms, a wide variety of complex
351 and varied spectra of powerful pulsations of magnetic and electric fields in the considered
352 frequency range considered here (ULF) can be generate in the geomagnetic trap, which are non-
353 regularly distributed over L ; these pulsations can lead to local acceleration and losses of the ERB
354 particles (see, e.g., Sauvaud et al., 2013). Such effects will violate the regular characteristics of the
355 protons distributions shown in Fig. 4 and 5. However, during quiet periods, the amplitudes of
356 such pulsations are small and they lead only to radial diffusion of particles.

357 4 Conclusions

358 On the basis of generalized Starting from the data on the fluxes of near-equatorial protons of the
359 ERB proton fluxes (with energy from $E \sim 0.2$ MeV to 100 MeV at and drift L shells L ranging
360 from ~ 1 to 8), their stationary distributions of the ERB protons over the drift frequency of
361 particles around the Earth (f_d) were constructed. The results of calculations of the number of
362 protons ΔN of the ERB protons within 30° in geomagnetic latitude at different L and f_d for periods
363 of maximum solar activity maximum are presented. They differ from the corresponding
364 distributions of the ERB protons for periods of low solar activity only at $L < 2.5$ (for comparison,
365 the spectra of these distributions are given at $L = 2$).

366 The radial profiles of these distributions $\Delta N(L, f_d)$ have only one maximum that shifts toward
367 the Earth with increasing f_d . In comparison to the proton fluxes profiles $J(L, E)$, the radial profiles
368 $\Delta N(L, f_d)$ at $f_d < 5$ mHz have steeper inner edges and flatter outer edges. However, the radial
369 profiles $\Delta N(L, f_d)$ at $f_d > 10$ mHz, which are formed by the CRAND mechanism, have inner and
370 outer edges with only slightly difference from each other for what concerns the steepness of
371 their profiles.

372 In contrast to the energy spectra of proton fluxes $J(E, L)$, the frequency spectra $\Delta N(f_d, L)$ of the
373 ERB protons at $L > 3$ are weakly dependent on L and, for sufficiently large f_d they have a nearly
374 power-law ~~form~~ **shape** with an exponent $\gamma = 4.71 \pm 0.43$. There is no local maximum in these
375 spectra in the region $\{f_d > 2 \text{ mHz}, L > 2.5\}$, as in the corresponding $J(E, L)$ spectra.

376 Distributions $\Delta N(L, f_d)$ and $\Delta N(f_d, L)$ of the ERB protons in the region $\{f_d > 0.5 \text{ mHz}, L > 3\}$
377 have a more ~~orderly form~~ **regular shape** than in the corresponding region of the space $\{E, L\}$, and
378 the main physical processes in the ERB manifested more clearly in these distributions. In these
379 regions, **there is most the majority** of the ERB protons, ~~are located~~ and their radial diffusion ~~of~~
380 ~~protons~~ overpowers their ionization losses during the transport of particles to the Earth.

381 In the region of the steep inner edges of the radial distributions $\Delta N(L, f_d)$, the spectra $\Delta N(f_d, L)$
382 of protons rapidly diverge from each other with decreasing L , and at low frequencies these spectra
383 become flatten. These results indicate a violation of the order in these distributions of protons
384 under the influence of ionization losses.

385 With increasing ~~in~~ solar activity, the number of protons $\Delta N(f_d, L)$ at $L \sim 2$ decreases for $f_d > 10$
386 mHz and increases for $f_d \sim 1\text{--}10$ mHz. The effect at high f_d , corresponding to protons with $E > 15$
387 MeV, is well known and is described in the framework of the CRAND mechanism.

388 However, the opposite effect, at low f_d corresponding to the lower-energy protons, is discovered
389 here for the first time. This effect can be associated with the fact that the low-frequency part of the
390 spectrum $\Delta N(f_d, L)$ of protons, even at $L \sim 2$, is **mainly** formed ~~mainly~~ by the mechanism of
391 protons transport from the outer regions of the ERB. This effect may indicate that with increasing
392 ~~of the~~ solar activity, the average rates of radial diffusion of protons increase **also as well**. For low-
393 energy protons at $L \sim 2$, the effect of increasing density of a dissipative medium with increasing
394 solar activity **is** overpowered by ~~the increasing~~ **increase of** the rates of radial diffusion of particles.
395

396 *Data availability.* All data from this investigation are presented in Figs. 1–5.

397 *Competing interests.* The author declares that there is no conflict of interest.

398 *Acknowledgements.* The author would like to thank the reviewers.

399

400

401 **References**

- 402 Alfvén, H., and Fälthammar, C.-G.: *Cosmical Electrodynamics, Fundamental Principles*,
403 Clarendon Press, Oxford, 1963.
- 404 Davis, L. R.: Low energy trapped protons and electrons, *Proc. Plasma Space Sci. Symp.*, Eds. D.
405 B. Chang and C. Y. Huang, Washington, P. 212–226, 1965.
- 406 Fennell, J. F., Blake, J. B., and Paulikas, G. A.: Geomagnetically trapped alpha particles, 3. Low-
407 altitude outer zone alpha-proton comparisons, *J. Geophys. Res.*, **79**(4), 521–528,
408 <https://doi.org/10.1029/JA079i004p00521> , 1974.
- 409 Fischer, H. M., Auschrat, V. W., and Wibberenz, G.: Angular distribution and energy spectra of
410 protons of energy $5 \leq E \leq 50$ MeV in the lower edge of the radiation belt in equatorial latitudes,
411 *J. Geophys. Res.*, **82**(4), 537–547, <https://doi.org/10.1029/JA082i004p00537>, 1977.
- 412 Fritz, T. A., and Spjeldvik, W. N.: Steady-state observations of geomagnetically trapped energetic
413 heavy ions and their implications for theory, *Planet. Space Sci.*, **29**(11), 1169–1193,
414 [https://doi.org/10.1016/0032-0633\(81\)90123-9](https://doi.org/10.1016/0032-0633(81)90123-9), 1981.
- 415 Garcia, H. A., and Spjeldvik, W. N.: Anisotropy characteristics of geomagnetically trapped ions, *J.*
416 *Geophys. Res.*, **90**(A1), 359–369, <https://doi.org/10.1029/JA090iA01p00359>, 1985.
- 417 Hoffman, R. A., and Bracken, P. A.: Magnetic effects of the quiet-time proton belt, *J. Geophys.*
418 *Res.*, **70**(15), 3541–3556, <https://doi.org/10.1029/JZ070i015p03541> , 1965.
- 419 Ilyin, B. D., Kuznetsov, S. N., Panasyuk, M. I., and Sosnovets, E. N.: Non-adiabatic effects and
420 boundary of the trapped protons in the Earth's radiation belts, *Bulletin of the Russian Academy*
421 *of Sciences: Physics*, **48**(11), 2200–2203, 1984.
- 422 Kovtyukh, A. S.: Relation between the pitch-angle and energy distributions of ions in the Earth's
423 radiation belts, *Geomagn. Aeron.*, **33**(4), 453–460, 1993.
- 424 Kovtyukh, A. S.: Geocorona of hot plasma, *Cosmic Res.*, **39**(6), 527–558,
425 <https://doi.org/10.1023/A:1013074126604>, 2001.
- 426 Kovtyukh, A. S.: Radial dependence of ionization losses of protons of the Earth's radiation belts,
427 *Ann. Geophys.*, **34**(1), 17–28, <https://doi.org/10.5194/angeo-34-17-2016>, 2016a.
- 428 Kovtyukh, A. S.: Deduction of the rates of radial diffusion of protons from the structure of the
429 Earth's radiation belts, *Ann. Geophys.*, **34**(11), 1085–1098, [https://doi.org/10.5194/angeo-34-](https://doi.org/10.5194/angeo-34-1085-2016)
430 [1085-2016](https://doi.org/10.5194/angeo-34-1085-2016), 2016b.
- 431 Kovtyukh, A. S.: Ion Composition of the Earth's Radiation Belts in the Range from 100 keV to
432 100 MeV/nucleon: Fifty Years of Research, *Space Sci. Rev.*, **214**(8), 124:1–124:30,
433 <https://doi.org/10.1007/s11214-018-0560-z>, 2018.
- 434 Kovtyukh, A. S.: Earth's radiation belts' ions: patterns of the spatial-energy structure and its solar-
435 cyclic variations, *Ann. Geophys.*, **38**(1), 137–147, [doi:10.5194/angeo-38-137-2020](https://doi.org/10.5194/angeo-38-137-2020), 2020.
- 436 Lejosne, S., and Kollmann, P.: Radiation Belt Radial Diffusion at Earth and Beyond, *Space Sci.*
437 *Rev.*, **216**(1), 19:1–19:78, <https://doi.org/10.1007/s11214-020-0642-6>, 2020.
- 438 Leonov, A., Cyamukungu, M., Cabrera, J., Leleux, P., Lemaire, J., Gregorie, G., Benck, S.,
439 Mikhailov, V., Bakaldin, A., Galper, A., Koldashov, S., Voronov, S., Casolino, M., De Pascale,
440 M., Picozza, P., Sparvulli, R., Ricci, M.: Pitch-angle distribution of trapped energetic protons
441 and helium isotop nuclei measured along the Resurs-01 No.4 LEO satellite, *Ann. Geophys.*,
442 **23**(8), 2983–2987, <https://doi.org/10.5194/angeo-23-2983-2005>, 2005.
- 443 Northrop, T. G.: *The Adiabatic Motion of Charged Particles*, Wiley-Interscience, NY, USA, 1963.
- 444 Parker, E. N.: Newtonian development of the dynamical properties of ionized gases of low density,
445 *Phys. Rev.*, **107**(4), 924–933. <https://doi.org/10.1103/PhysRev.107.924>, 1957.
- 446 Roederer, J. G.: *Dynamics of Geomagnetically Trapped Radiation*, Springer, NY, USA, 1970.
- 447 Sauvaud, J.-A., Walt, M., Delcourt, D., Benoist, C., Penou, E., Chen, Y., and Russell C. T.: Inner
448 radiation belt particle acceleration and energy structuring by drift resonance with ULF waves

449 during geomagnetic storms, *J. Geophys. Res. Space Physics*, **118**(4), 1723–1736,
450 <https://doi.org/10.1002/jgra.50125>, 2013.

451 Selesnick, R. S., Looper, M. D., and Mewaldt, R. A.: A theoretical model of the inner proton
452 radiation belt, *Space Weather*, **5**(4), S04003, <https://doi.org/10.1029/2006SW000275>, 2007.

453 Selesnick, R. S., Hudson, M. K., and Kress B. T.: Direct observation of the CRAND proton
454 radiation belt source, *J. Geophys. Res. Space Phys.*, **118**(12), 7532–7537,
455 <https://doi.org/10.1002/2013JA019338>, 2013.

456 Selesnick, R. S., Baker, D. N., Jaynes, A. N., Li, X., Kanekal, S. G., Hudson, M. K., and Kress, B.
457 T.: Observations of the inner radiation belt: CRAND and trapped solar protons, *J. Geophys.*
458 *Res. Space Phys.*, **119**(8), 6541–6552, <https://doi.org/10.1002/2014JA020188>, 2014.

459 Selesnick, R. S., Baker, D. N., Kanekal, S. G., Hoxie, V. C., and Li, X.: Modeling the proton
460 radiation belt with Van Allen Probes Relativistic Electron-Proton Telescope data, *J. Geophys.*
461 *Res. Space Phys.*, **123**(1), 685–697, <https://doi.org/10.1002/2017JA024661>, 2018.

462 Shi, R., Summers, D., Ni, B., Manweiler, J. W., Mitchell, D. G., and Lanzerotti, L. J.: A statistical
463 study of proton pitch-angle distributions measured by the Radiation Belt Storm Probes Ion
464 Composition Experiment, *J. Geophys. Res. Space Phys.*, **121**(6), 5233–5249,
465 <https://doi.org/10.1002/2015JA022140>, 2016.

466 Søråas, F., and Davis, L.R.: Temporal variations of 100 keV to 1700 keV trapped protons observed
467 on satellite Explorer 26 during first half of 1965, Rep. X-612-68-328, NASA Goddard Space
468 Flight Cent., Greenbelt, Md., 1968.

469 Williams, D. J., and Lyons, L. R.: The proton ring current and its interaction with plasmopause:
470 Storm recovery phase, *J. Geophys. Res.*, **79**(28), 4195–4207,
471 <https://doi.org/10.1029/JA079i028p04195>, 1974.

472 Williams, D. J., and Frank, L. A.: Intense low-energy ion populations at low equatorial altitude, *J.*
473 *Geophys. Res.*, **89**(A6), 3903–3911, <https://doi.org/10.1029/JA089iA06p03903>, 1984.